

## **Static and Dynamic Fracture of Transparent Nanograined Alumina**

A. Belenky<sup>1</sup>, I. Bar-On<sup>2</sup> and D. Rittel<sup>1\*</sup>

1. Faculty of Mechanical Engineering, Technion, 32000 Haifa, Israel

2. Dept. of Mechanical Engineering, Worcester Polytechnic Institute, Worcester, USA

### **Abstract**

Transparent nanograined alumina has a great technological potential for highly demanding applications which take advantage of its superior mechanical properties like hardness, wear resistance and strength, in addition to its optical performance in the infrared and visible domain. Accurate fracture properties (toughness) of this material are rather scarce in the quasi-static regime, and almost non-existent in the dynamic regime. Therefore, the present work investigates the static and dynamic fracture toughness of polycrystalline, nanograined alumina. The results show a marked increase in the dynamic initiation toughness when compared with the quasi-static regime, a phenomenon that was previously observed for other quasi-brittle materials. A combined fractographic and numerical study is carried out in order to identify the underlying mechanism(s) for the observed high dynamic initiation toughness. It is proposed that the latter results from the combined effect of a geometrical crack-front perturbation along with the contribution of the kinetic energy of the specimen. A discussion of the dynamic fracture toughness as a material property concludes this work.

\* Corresponding autor: merittel@technion.ac.il

## 1. Introduction

Static and dynamic fracture resistance of engineering materials has drawn much attention in last decades. Many sophisticated engineering structures, e.g. high pressure vessels, aerospace and power generation parts, are designed to withstand cracks. The need for high-performance materials in such industries has integrated the use of fracture toughness data in design considerations. In particular, fracture toughness is used on regular basis as a design parameter to insure safety performance of the mechanical equipment. The American Society for Testing and Materials (ASTM) has issued detailed standards for static fracture testing, e.g. ASTM E399 (1990) and ASTM C1421 (1999), when the first is for metals and the second for advanced ceramics. Static fracture toughness characterization of advanced ceramic materials is relatively well established, with many techniques being available, Gogotsi (2003). The ASTM C1421 (1999) standard suggests three different standardized techniques for the determination of the critical static fracture toughness for advanced ceramics, namely: single-edge precracked beam (SEPB), surface crack in flexure method (SCF), and the chevron-notched beam method (CNB). All these methods are relatively similar except for the definition and introduction of the initial precrack that must be as sharp as possible.

By contrast, the dynamic fracture toughness concept has been less investigated and there is no widely accepted simple and reliable procedure, or even standard for the determination of the dynamic fracture toughness. Yet, many engineering structures are subjected to impact loadings, and there is a need to assess them for potential crack propagation. Several techniques for the determination of dynamic stress intensity factor have been proposed over the past three decades, which can be roughly categorized into three main groups: high rate bending, high rate tension, and dynamic wedging, (Shukla (2006) or Jiang and Vecchio (2009)). In the recent years, the one-point impact technique has gained momentum due to its simplicity (Rittel, 2006). The idea is to impact a free-free cracked beam that fractures by inertia, while measuring the fracture time by means of single-wire fracture gauges, (Weisbrod and Rittel, 2000). This method has been applied to various quasi-brittle materials, such as polymethylmethacrylate, (Rittel and Maigre, 1996), ceramic composites, (Rittel, et al., 2005), A508 steel ((Rittel, et al., 2002b)), tungsten base heavy alloys, (Rittel and Weisbrod, 2001), and a beryllium

based bulk metallic glass (BMG), (Rittel and Rosakis, 2005) for which a comparison was made between this method and the full field method of Coherent Gradient Sensing. Rittel and Rosakis (2005) found that two radically different techniques yielded very similar results for the impact fracture toughness of their BMG.

One of the key issues in dynamic fracture testing lies in the discrepancy between static and dynamic initiation fracture toughness values. Some materials may not exhibit a distinct rate sensitivity such as 7075-T6 aluminum alloy, (Yokoyama, 1993). Yet, this author also reports in the same paper that the dynamic fracture toughness of the Ti-6246 alloy and 4340 steel is 50% and 40% higher, respectively, than the corresponding quasi-static fracture toughness. However, more recent works show that other materials do show a significant difference between the static and dynamic fracture toughness. For example, the study of Rittel and Maigre (1996) shows that the dynamic fracture toughness of PMMA is more than three times higher than the static one. These authors proposed that, the increase of initiation fracture toughness is caused by multiple microcracks formed around the crack tip, whose dynamic coalescence with the main crack tip delays the onset of crack initiation, thereby increasing the measured initiation toughness. For a commercial tungsten base heavy alloy, Rittel and Weisbrod (2001) report a 30% increase, and for Vitreloy-1 (BMG), Rittel and Rosakis (2005) report a highly rate sensitive initiation toughness. The physical reasons for the observed difference have not been elucidated yet.

Kalthoff (1986) explained those differences by postulating the existence of a fracture incubation time, during which the effective stress intensity factor increases rapidly above its quasi-static value. Aoki and Kimura (1993) found that there is a delay time to detect crack initiation on the outer surfaces of the specimen, and this delay may result from the fact, that the stress intensity factor at the mid-thickness of the specimen is higher than that on the surface, and that the difference is larger for dynamic loading. It has also been proposed that the high toughness values can be attributed to the time required to establish a singular crack-tip field as compared to the actual fracture time (Liu, et al., 1998; Zhang and Gross, 1992). Fracture in the absence of a singular field would render the material apparently tougher. However, the characteristic times corresponding to this situation are extremely short compared to the actual fracture times recorded in an experiment, so that this point won't be dealt further. Another physical

explanation is that the actual crack front shape might have some roughness or irregularities, as revealed by post-mortem fractographic investigation of fracture surfaces. A similar phenomenon was also identified by Rittel et al. (2005), and Kaplan et al. (2004) for an infiltrated TiC-1080 steel cermet. A distinct crack-tip morphology was also reported by Rittel and Rosakis (2005) for an amorphous alloy. From a theoretical point of view, Gao and Rice (1989) analyzed the effect of toughness heterogeneity along the crack-front, coupled to a weak geometrical perturbation, predicting a significant toughening effect. More generally, the subject of crack front perturbations and the influence of local variations in fracture toughness have been addressed from a statistical physics point of view in terms of crack depinning from local obstacles, (Ponson, 2009). However, aside from considering quasi-static fracture, most works concentrates on propagating cracks. An interesting result is that the energy dissipation increases markedly with the crack velocity, a fact that is explained by the increasing process zone size, (Broberg, 2002).

To summarize, it seems that the dynamic initiation toughness of quasi-brittle materials is significantly higher than its quasi-static counterpart and the underlying reason can be traced to specific dynamic failure micromechanisms which are equivalent to crack-tip damage whose role is to delay the propagation of the main crack front.

Currently, most of the evaluation techniques to determine the dynamic fracture toughness of the material are limited to outer surface measurements on the specimens (fracture gauges or high speed photography with optical techniques) and post-mortem investigations of fracture surfaces. The lack of the ability to see what actually happens at mid thickness of the specimen during crack initiation and advance hamper our full understanding of the observed discrepancy.

This paper reports data for the quasi-static and dynamic initiation toughness of transparent nanograined alumina, along with an attempt to model and explain the physical reasons for the observed increased dynamic values.

The paper is therefore divided into three main sections. The first section describes the investigated material, the hybrid experimental-numerical procedure both in static and dynamic loading conditions, and the measured toughness results. The second section reports a detailed fractographic study of the failure micromechanisms. The third section

introduces numerical simulations of a perturbed crack front, followed by a discussion of the dynamic fracture toughness as a material property.

## **2. Material and specimens**

Nanograined alumina plates that were used in this study were prepared by CeraNova, MA, USA by using powder metallurgy and described in details in Parish et al. (2005), Note that a similar material was also previously elaborated by Krell et al. (2003a). According to the manufacturer, the material is close to full density, with a mean grain size of 0.7  $\mu\text{m}$ , and hardness, HV(1), of  $2284 \pm 53$  [kgf/mm<sup>2</sup>], (Parish, et al., 2005). Additional properties are listed in Table 1.

Bend bar specimens ( $6 \times 8 \times 45$  mm<sup>3</sup>), were cut from these plates (Figure 1). All the faces of the specimens were initially ground and edges were chamfered according to standard requirements, (ASTM-C1421, 1999). The faces for the indents were polished to a mirror finish (0.1  $\mu\text{m}$ ). Precracks were introduced following ASTM C1421 (1999) recommendations. Namely, the specimen was indented using a Vickers indenter which resulted in 4 microcracks, one at each tip of the indentation, as shown in Figure 2a. Subsequent controlled bending was carefully applied to allow for controlled growth of two of these microcracks into a full thickness sharp crack whose length was measured using an optical microscope, (Figure 2b). Figure 2b was obtained with specimen trough lightning, emphasizing the translucency of the nanograined PCA (polycrystalline alumina). By controlling the Vickers indentation load and the bridge span of the double anvil fixture (Figure 3) one can control the length of the precrack that will be introduced into the specimen, (Baron, et al., 1990). Precrack straightness was found to depend on the initial surface roughness. The specimens were initially ground by the manufacturer, to a mean roughness of Ra 0.2  $\mu\text{m}$  and then polished to Ra 0.1  $\mu\text{m}$  or better. All roughness measurements were performed on a Wyko NT1100 interferometer. The specimens with Ra<0.1  $\mu\text{m}$  tend to develop straighter precracks than specimens with greater Ra. The dependency of fracture toughness values on precrack straightness was investigated by Grendahl et al. (2000) who observed that deviations from straightness may cause inflated values of the measured static fracture toughness values, so that great care should be taken in order to keep the precrack as

straight as possible. The same technique of sharp precracking was used for both the static and dynamic tests, noting in passing that for dynamic testing of ceramics, this technique was not used previously to the best of our knowledge. Because of the limited number of bend bar specimens for the dynamic tests, half-specimens ( $6 \times 8 \times 22.5 \text{ mm}^3$ ) that remained from the previous fracture tests, were again precracked and tested.

### **3. Experimental setup and procedures**

#### **3.1 Static tests.**

The specimens were fractured in three-point bending with a span to width ratio of 5, Figure 4, at a loading rate of 0.5 mm/min in an Instron 4483 with 500N load cell, under displacement control. The fracture toughness was calculated from the maximum load and crack length measurements, according to standard recommendations, (ASTM-C1421, 1999). There was no evidence of R-curve behavior for this material as expected.

#### **3.2 Dynamic tests.**

For the dynamic experiments reported in this paper, a modified Split Hopkinson (Kolsky) Pressure Bar (SHPB), (Kolsky, 1949), was used with one-point impact configuration technique, as shown in Figure 5. A detailed overview of this method can be found in Weisbrod and Rittel (2000). The minor difference between the techniques used by Weisbrod and Rittel (2000) and that implemented in this study, is that their metallic specimens were sharp-notched and fatigue precracked with almost the same crack length, while the specimens of this study had a varying initial crack length. Therefore, each dynamically broken specimen was numerically simulated using the actual force measured during an impact, as opposed to one generic simulation and convolution with the applied load, as in Weisbrod and Rittel (2000). Single wire fracture gauges were silk-screened on each side of the specimens in the vicinity of the crack tip using silver paint, (Figure 6). The gauges were wired to a power source and a digital oscilloscope, so that crack initiation time was detected during the impact test. A typical experimental record consists of incident and reflected pulses, collected from the strain gauges mounted on the middle of the incident bar, as well as two fracture gauges'

signals (Figure 7a and after data reduction Figure 7b). All the signals were synchronized with the incident strain gauge signal. Before testing the alumina specimens, preliminary tests and calculation routines were made on sharply notched PMMA specimens of identical dimensions. PMMA material was chosen because of the availability of static and dynamic fracture toughness data, (Rittel and Maigre, 1996), and as shown in the sequel, this calibration step was passed successfully.

A 2D plane strain finite element model (ABAQUS, 2008), was used to calculate the dynamic stress intensity factor (DSIF) for each specimen as a function of time using Irwin's formula which relates the crack opening displacement (COD) to the DSIF. Numerical convergence of the model and the validity of LEFM and SSY assumption were checked both for PMMA and PCA specimens. A meshed 2D plain strain alumina half-specimen along with the boundary conditions is shown in Figure 8. Except for the symmetry condition, all other boundary conditions were set free-free. It was previously shown by Giovanola (1986) and by Rittel et al. (2002a) that an impacted unsupported structure will not immediately start to propagate upon impact. Rather, a certain amount of time will elapse, during which loading waves travel back and forth in the structure, and the structure fractures long before the specimen taking off from the contact with the incident bar. The acting force was modeled as a pressure pulse. The measured fracture time was used to calculate the exact value of the dynamic fracture toughness. The  $K_{Id}$  values for PMMA specimens, shown in Figure 9, were found to be in good agreement with previous results, (Rittel and Maigre, 1996), thus validating the adopted experimental approach.

## 4. Experimental results

### 4.1 Static fracture

Table 2 summarizes the static fracture toughness results of this study and compares these to the Indentation Fracture Toughness (IF) results of identical and similar materials. The second row shows the results of indentation fracture measurements for an identical material that were reported by the manufacturer, (Parish, et al., 2005) , and the third row shows results for a similar nanograined Alumina, (Krell, et al., 2003b). It can be seen that the current results tend to be slightly lower as would be expected for a

straight crack. In order to get additional data for comparison, an attempt was made to calculate the IF values. First, Vickers hardness measurements were made on Mitutoyo MVK-H1 micro hardness testing machine. The indentation load was 1 kgf. The measurements and calculations of Vickers hardness were made according to ASTM C1327 (1999), "Standard Test Method for Vickers Indentation Hardness of Advanced Ceramics". The measurements of the diagonal length of Vickers indentation and cracks length that emanate from the corners of the indentation are delicate due to the translucency of the indented material. The measured hardness, HV(1), is  $2364 \pm 170$  ( $\pm 7.5\%$ ). Several empirical equations were used to determine the indentation toughness, but the results were not consistent or even close to the results that were measured by the standardized technique or reported by other authors. Therefore, our indentation toughness values will not be reported here. It should be emphasized that recent work of Quinn and Bradt (2007) suggests that the IF technique may not be the most suitable technique to measure reliably the true fracture toughness of a material.

Measured SEPB static fracture toughness values versus non-dimensional crack length are shown in Figure 10. The green dashed line shows the average fracture toughness value of  $3.12 \pm 0.075 \left[ MPa \cdot \sqrt{m} \right]$  from 9 measurements. According to the plot, there is no evidence for R-curve behavior, and Figure 10 clearly shows that the relative initial crack length does not affect the measured SEPB fracture toughness values.

#### 4.2 Dynamic fracture

The dynamic fracture toughness values of nanograined PCA and comparison with static fracture toughness are summarized Table 3. In this table one also can find some reference results for other ceramic materials. The results for SiC-N by Weerasooriya et al. (2006), - second row in Table 3 - clearly indicate the same trend for the dynamic toughness values, but the stress intensity rate that is reported by these authors is markedly lower than ours. Additional results for Alumina with average grain size of 3  $\mu m$  are also summarized in the third row of Table 3, (Suresh, et al., 1990). These results contradict the present values and also the whole trend presented here. The reason for those discrepancies is that these authors used the maximum load to calculate their dynamic fracture toughness values with no attempt to accurately measure a true time to fracture. However, it is a well established fact that fracture typically happens beyond



the maximum value of the force, as a result of inertial effects, so that the peak load cannot be identified as an indication of fracture, (Rittel, et al., 2002a). This is clearly shown in Figure 7b where one can note the excellent agreement between the two fracture gauges' readings. For PCA Alumina, the typical fracture time was measured between 12 to 18  $\mu s$ , and for PMMA specimens the fracture time was between 22 to 26  $\mu s$ . As mentioned before, (Rittel, et al., 2002a), the accurate timing of fracture is a critical issue. The (stress intensity) rate-sensitivity of the fracture toughness is summarized in Figure 11, showing a good agreement with the trend reported by Weerasooriya et al (2006).

At this stage, one should note that the results of the dynamic fracture toughness for both materials, PMMA and PCA, contain a built-in experimental error. The main source of the error lies in the accurate detection and timing of the onset of crack propagation, as indicated by the fracture of the fracture gauge. In addition, if the crack nucleates at mid-thickness of the specimen, some time will be required until it reaches the outer surface where the fracture gauges are cemented (Aoki and Kimura, 1993). The latter effect cannot be presently quantified. As to the crack-fracture gauge position, note that the crack-tip is at most positioned 0.25 mm ahead from the crack-tip (Figure 6). Assuming a low crack propagation velocity of 200 m/s at initiation, the resulting delay time is  $t_{err} = 1\mu s$ . Consequently, the resulting error will be of  $K_{err} = -t \times \dot{K}$ . The minus sign expresses the overestimation of the fracture toughness. Note that  $t_{err} = 1\mu s$  is highly conservative, as cracks run faster at higher initiation toughness. In Figures (9) and (11), the actual toughness values will therefore be slightly lower than those plotted due to the above-mentioned error.

## 5. Characterization of the failure mechanisms

A comparison of fractographic pictures of selected areas of the dynamically and statically broken specimens, at similar magnifications is shown in Figure 12. The solid arrow shows the fracture direction. Pictures D1-D3, left column, show different areas of a dynamically broken specimen (Sp1-2). Pictures S1-S3, right column, show different areas of a statically broken specimen (Sp2). D3 and S3 show the precracked region. D2 and S2 show the transition region between the precrack and its extension. The white

dashed line on picture D2 outlines a distinct difference in failure mechanism between the precrack and the crack in its initiation stage, whereas there is no such distinct difference for the statically broken specimen. D1 and S1 show the typical morphology of the fracture surface at about 1 mm away from the initiation line. Two distinct failure mechanisms are identified, namely transgranular ("T") and intergranular ("I") fracture. The failure mechanism in the precrack, is predominantly transgranular, but near the end of the precrack intergranular failure becomes dominant, as shown in the bottom of picture S2. For the static specimen, the lack of difference between the precrack and its extension was already reported by Nose and Fujii (1988). This is not the case for the dynamic specimen (D2). Here, as outlined by the dashed white line, the precrack looks mostly intergranular, while the initiation area is essentially of a transgranular nature with a minor intergranular component. Once the crack has propagated over some 100  $\mu\text{m}$ , the fracture surface is mostly intergranular, so that the propagation regime of a static and a dynamic specimen are virtually undistinguishable from a sole fractographic point of view. Those pictures of fracture surfaces and the precrack are found to be repeatable and therefore characteristic for each loading regime. Therefore, a preliminary conclusion about the differences in fracture toughness values at different rates can be made, namely that a unique fracture initiation mechanism (transgranular) is observed to operate in the dynamic regime, which does not operate in the quasi-static case. One can note here that qualitatively similar observations were reported by Rittel and Maigre (1996) for PMMA, for which once the crack had started to propagate, the topography of the dynamic and static fracture surfaces was virtually identical. In other words, a unique fracture mechanism is observed to characterize the highly transient initial phase of the dynamic crack initiation in the investigated ceramic.

## 6. Numerical simulations and analyses

### 6.1 Foreword

The fractographic study clearly reveals a mixed transgranular / intergranular zone at the origin of the dynamic crack. Such a mixture can be modeled in terms of a perturbation of the fracture toughness due to two distinct fracture mechanisms. Indeed, basic results have been established for such as case, considering quasi-static fracture. However,

while those analyses clearly point out to a toughening effect due to the perturbed crack-front, one cannot really apply them directly to the present case for which the exact values of the toughness corresponding to each mechanisms are unknown so far, except for the intergranular mechanisms that operates in the quasi-static regime, if one considers it to be rate-independent.

Therefore an alternative way to look at this problem in a generic form is to consider a geometric perturbation of the otherwise straight crack-front. Such a perturbation would correspond to parts of the crack front that are “pinned” by the high toughness region as opposed to those that propagate in view of the lower local toughness. Generic results for a geometric perturbation are not available to the best of our knowledge. Therefore, in this section, we investigate the effect of a geometrical perturbation in a quite general manner, which is not necessarily that observed here. The crack front can be either straight (unperturbed) or comprise triangular sections to represent a tendency for selective advance of certain segments as discussed before. The idea of the simulation is to ascertain the toughening (or weakening) effect of such perturbations, both in the quasi-static and in the dynamic regime.

## 6.2 Theoretical considerations

The goal here is to understand the influence of the crack front shape on the energy release rate  $G$ , with the underlying assumption that the critical energy release rate corresponds to the fracture toughness of the material, the latter being an increasing function of the crack-velocity and/or roughness, (Broberg, 2002). Various combinations for the crack progression schemes are investigated, namely straight-straight, straight-triangle and triangle-straight (Figure 13). In the case of a straight crack front before and after propagation, the energy release rate is calculated in a straightforward manner. For triangular crack front shapes, before or after propagation, an "energy release rate criterion" ( $G^*$ ) is suggested and calculated.

The definition of the energy release rate is given by:

$$G = -\frac{\partial \Pi}{\partial A} = \lim_{\Delta A \rightarrow 0} -\frac{\Delta \Pi}{\Delta A} \quad (6.1)$$

Where  $\Pi$  is the potential energy and  $A$  is the crack area,  $\partial/\partial A$  is partial derivative with respect to crack area. In order to use this definition, two numerical states should be

evaluated. The only difference between the two states is the crack area and crack front shape. The first state is supposed to represent the initial crack front shape and area. The second state is representing the final crack front shape and area after a small crack propagation increment for which  $\Delta A \rightarrow 0$ . By calculating numerically the potential energy for the two states and knowing  $\Delta A$ , an estimation of the energy release rate can be calculated, according to equation (6.1).

By definition, the energy release rate is a measure of the energy available for an increment of crack extension and it also called the crack extension force or crack driving force, (Gdoutos, 2005). For the static loading regime the definition of energy release rate can be simplified to the next form, (load control):

$$G = -\frac{\partial \Pi}{\partial A} = \lim_{\Delta A \rightarrow 0} -\frac{\Delta \Pi}{\Delta A} \cong -\frac{[(U_2 - 2U_1) - (U_1 - 2U_1)]}{\Delta A} = \frac{U_2 - U_1}{\Delta A} = \frac{\Delta U}{\Delta A} \quad (6.2)$$

Knowing the elastic fields,  $U_1$  and  $U_2$ , of two equilibrium states 1 and 2, where the first corresponds to crack area  $A$  and the second to  $A + dA$ , with the same prescribed loads, the energy release rate may be approximated by equation (6.2).

The definition of the dynamic path-independent  $J_d$ -integral (which also is the energy release rate,  $J_d = G_d$ ) according to Anderson (1995) is different from the static case and inertial effects should be taken into account:

$$G(t) = -\frac{\partial \Pi}{\partial A} = -\left( \frac{\partial F}{\partial A} - \frac{\partial U}{\partial A} - \frac{\partial E^k}{\partial A} \right) \quad (6.3)$$

Where  $F$  is the work done by the external forces,  $A$  and  $U$  are as mentioned above,  $E^k$  is the kinetic energy. Equation (6.3) can therefore be re-written as:

$$G(t) = \lim_{dA \rightarrow 0} \left[ -\left( \frac{F_2 - F_1}{dA} - \frac{U_2 - U_1}{dA} - \frac{E_2^k - E_1^k}{dA} \right) \right] \quad (6.4)$$

Assuming the same prescribed loads ( $F_1 = F_2$ ), the first term in equation (6.4) vanishes, so that the dynamic energy release rate may now be approximated by:

$$G(t) = \lim_{dA \rightarrow 0} \left[ \frac{U_2 - U_1}{dA} + \frac{E_2^k - E_1^k}{dA} \right] \quad (6.5)$$

For the general case of crack advance, both for triangular and for straight crack fronts:

$$G^*(t) \approx \frac{\Delta U + \Delta E^k}{\Delta A} \quad (6.6)$$

An examination of the equation (6.6) leads to the conclusion that the term  $\frac{dE_k}{dA}$ , if positive, has a toughening effect on the material as pointed out by Chandra and Krauthammer (1995).

### 6.3 The model for a geometrical crack-front perturbation

A total of 5 combinations consisting of two types (states) of crack front shape and area (before and after propagation), were considered in present work. For the sake of brevity, it will be reported that out of the 5 combination of crack front initiation and advance that were considered (straight-straight, straight-fully triangular, straight-two triangles, two triangles-straight, fully triangular-straight), only 3 have a physical meaning, as shown on Figures 13 (a-c). Namely, two combinations: straight-fully triangular and straight-two triangles, resulted in a negative energy release rate, indicating that crack propagation is not feasible for those schemes, in both the static and dynamic loading regimes.

The problem was modeled numerically using commercial finite element code ABAQUS 6.8 (2008), and the material was modeled as isotropic linear elastic (Table 1). Because of two symmetries only one quarter of the specimen was modeled, as shown in Figure 14. For the static loading the model was constrained on a short strip in the bottom surface, and the load (pressure) was applied on the finite strip on the top surface, as close as possible to the 3-point bending configuration. For the dynamic loading the boundary conditions were set free-free, and the force acts like a pressure on the equivalent area on the bottom surface, as partially described in section 3.2 and Figure 8. The element type, the analyses' type, number of elements and characteristic element size that was used for each kind of crack front and loading regimes are all summarized in Table 4.

The load which was applied numerically is the one which was measured experimentally, for static and dynamic loadings, respectively. To check numerical consistency and convergence, the energy release rate calculated numerically (equation 6.1) was compared to  $G$  determined from  $K_I$  (linear elastic equivalence), the latter being calculated from the crack face displacements, for quasi-static and dynamic cases as

well. The energies extracted from the numerical simulation were used to calculate the energy release rate or energy term, depending on the type of crack front. For the case of the dynamic loading, the energy values were taken on the exact time of fracture, as shown in Figure 15. During the dynamic loading simulation energy conservation was checked, dotted line in Figure 15. The total energy was calculated as subtraction of the kinetic and strain energies from the work done by external forces during the impact. Zero total energy during the simulations shows overall conservation of energy, thus validating the simulation model.

#### 6.4 Numerical results

Figure 16 shows the calculated energy release rate ( $G$ ) and energy criterion ( $G^*$ ) as a function of the normalized crack area increment for the static and dynamic loading, considering various crack-front geometries. The following cases are considered: 1.1 – straight-straight, 2.1 – fully triangular-straight, and 3.1 – two triangles-straight. The toughness is the extrapolated value of the curves to a vanishing increment of crack area. It is first noted that for the case of straight-straight crack front propagation (case 1.1), an excellent agreement is obtained with the experimental results for the two loading regimes, when  $\Delta A \rightarrow 0$ . This agreement is expected and it validates in fact the overall simulation method. It also appears that, irrespective of the case considered, there is a definite qualitative similarity in the toughness-crack increment curves for the two loading regimes, while the dynamic values are clearly higher than the quasi-static ones. For a geometrically unperturbed crack-front (case 1.1), the increased dynamic toughness is obviously the result of the kinetic energy term alone. When the crack-front is perturbed, the exact nature of the perturbation does not seem to affect the values of the toughness in each regime. Yet, the perturbation itself clearly contributes significantly to elevate the toughness above the reference value obtained for a straight-straight propagation case. A better understanding of the influence of the nature of the perturbation is obtained by re-plotting Figure 16 using linear axes (Figure 17). Comparing cases 2.1 and 3.1, when the former contain denser geometrical irregularities than the latter, one can conclude that denser geometrical irregularities tend to increase  $G$  and  $G^*$ . This phenomenon may be explained by checking equation (6.2) for static loading or equation (6.6) for the dynamic loading. Both equations contain in the

denominator the term  $\Delta A$ , when denser irregularities make it smaller, thereby increasing  $G$  and  $G^*$ .

At this stage, one should remark that no experimental evidence was found for the existence of cases 2.1s and 3.1s, so that the results brought here for these cases do not bear a definite physical meaning, contrary to the dynamic case.

The kinetic energy term is causing a noticeable elevation of the fracture toughness (extrapolation of the curves to  $\Delta A \rightarrow 0$ ) in the dynamic case, Figure 16. Table 5 summarizes typical values of the toughness for the various investigated cases. In the dynamic straight-straight case, the kinetic term  $\Delta E^k / \Delta A$  is 0.94 of to the measured toughness  $G^*$ , which becomes 0.62 when the crack-front is fully made of triangles.

One can now summarize the main results of the numerical simulations by stating that a positive contribution (toughening) of the kinetic energy term has been observed in addition to that of the geometrical crack-front perturbation. Since this contribution is inversely proportional to  $\Delta A$ , the finer the perturbation the higher the additional contribution to the overall toughness. These results apply to the quasi-static and dynamic case, when for the former, only straight-straight propagation is observed.

## 7. Discussion

This work concerns the static and dynamic initiation fracture toughness properties of transparent nanograined polycrystalline alumina. An accurate methodology was applied, which includes the generation of sharp cracks, for the determination of this property. From an experimental point of view, the selected approach overcomes problems related to the crack-tip sharpness and the usual approximations made during indentation toughness testing.

The measured values of the quasi-static toughness of this material were not previously reported, even if they are perfectly in line with the expectations from a ceramic material (Parish et al., (2005) and Krell et al., (2003b)). As a preliminary remark, one should note that all the results point to the fact that initiation fracture toughness of PCA is distinctly rate-sensitive, showing a marked increase in the dynamic versus quasi-static regime. As a typical figure, the dynamic initiation toughness is about one order of magnitude greater than its quasi-static counterpart. Such a result, although surprising at

first sight, has already been observed in other quasi-brittle materials, (Rittel and Rosakis, 2005), and just confirms what seems to be a consistent trend for these materials, whether amorphous or crystalline. The elucidation of this point was quite central in this work.

A first step was to carefully compare the topography of the fracture surfaces in the immediate vicinity of the precrack. In the quasi-static regime, no new failure mechanism is observed, other than intergranular fracture which prevails at initiation and at the later stages of propagation. However, for the dynamically broken specimens, one clearly observes over a depth of about 100  $\mu\text{m}$  from the end of the precrack a unique region which consists of a dominant transgranular component with interspersed islands of intergranular fracture. Away from this region, the fracture proceeds in an intergranular mode, much similar to that observed in the propagation phase of the quasi-static specimens. The observation of a distinct failure mechanism in the dynamic initiation zone has also been reported for several quasi-brittle materials with high dynamic initiation toughness. Consequently, one can partly attribute the elevated dynamic toughness to this unique failure micromechanism. In this general context, one should again mention the work of Gao and Rice (1989) who showed that different distributions of tough particles may temporary block crack advance, so that the local fracture toughness may increase (limited in their study to up to twice). However, their study was limited to a first-order theory and the maximum perturbation of the crack front was kept within a reasonable range. Here, two important points need to be considered. The first is the very influence of the loading rate itself, while the second relates to the mixed failure mechanisms in a well defined zone.

In this work, we decided to model this observation as a geometrical perturbation of the crack front, in an attempt to mimic the fact that, since two toughness levels are clearly present, the initially straight crack-front cannot dynamically propagate in a self-similar fashion. The subject of crack-front perturbations is well documented in the quasi-static regime with emphasis on a coupled geometrical-material perturbation, through the varying toughness. However, the current work lumps the mixed perturbation into a solely geometrical perturbation, to assess the joint influences of the loading rate and the geometry, in the absence of reliable data for the toughness of each failure mechanism.



Numerical simulations were carried out on various idealized crack front geometries, using measured loading data and fracture time. This assumption has to be made since one cannot decouple the measured load and fracture time from the crack-front geometry. In other words, the latter actually dictates the two former parameters. Within this context, the numerical results clearly point out a “toughening” role of the kinetic energy associated with the process.

The next observation is the added contribution of the geometrical perturbation itself, only for the dynamic loading case. A general trend is that the finer the perturbation in geometrical terms, the higher its contribution to the toughening. Therefore, in the dynamic regime, two distinct contributions to the observed toughening are now identified, namely kinetic and geometrical. These mechanisms are deemed to be responsible for the very high measured apparent toughness values of quasi-brittle materials like the PCA of this work. Note that we deliberately introduced the geometrical perturbations in the plane of the crack instead of introducing an additional degree of freedom, namely out of plane perturbations, which are closer to the physical observations of a rough crack front. Three dimensional perturbations are indeed more realistic, however, to be representative, they should be added in a statistical way which significantly expands the numerical work to a point that justifies a separate study. It is believed that the current two-dimensional perturbations are sufficient to illustrate the nature of the toughening process in the current framework.

At this stage, one important question arises, namely: is the measured dynamic fracture toughness a material property or is it the simple outcome of the kinetic energy term which is essentially structural? To answer this question, one should look again at Figure 9, in which fracture toughness values are reported for commercial PMMA, as measured using two radically different test geometries, namely Compact Compression Specimens (CCS) and the present short beams. From this figure, neglecting the experimental scatter, one can see that the measured toughness values for two radically different specimen geometries all lie in a common range of values,  $4 \times 10^4 \leq \dot{K} \leq 8 \times 10^5 \text{ MPa}\sqrt{m}/s$  and  $2 \leq K \leq 6 \text{ MPa}\sqrt{m}$ . The same observation can be also made for PCA specimens, (Figure 11). Again, despite the scatter in dynamic toughness values, the two beam specimen geometries used here, long and short beams, show overlapping results for  $4 \times 10^6 \leq \dot{K} \leq 2 \times 10^7 \text{ MPa}\sqrt{m}$  and  $25 \leq K \leq 40 \text{ MPa}\sqrt{m}$ .

One should note here that a similar scatter in fracture toughness values is frequently observed, e.g. for steels in the brittle (lower shelf) regime, (Ritchie, et al., 1973). These observations suggest that since the fracture toughness is independent of the specimen geometry to a first extent, it may very well be a real material property, just like it is in the quasi-static case. This question was not addressed previously to the best of our knowledge and the present suggestion would require additional testing and validation in the spirit of the experiments presented here.

## 8. Conclusions

The static and dynamic initiation fracture toughness were measured and modeled numerically, and the main conclusions as follows:

1. Static fracture toughness of nanograined PCA is  $3.12 \pm 0.075 [MPa\sqrt{m}]$ .
2. No R-curve behavior was found and the relative initial crack length does not affect the measured SEPB fracture toughness values.
3. The same technique of sharp precracking was used for both the static and dynamic tests, noting in passing that for dynamic testing of ceramics, this technique was not used previously to the best of our knowledge.
4. Dynamic initiation fracture toughness of nanograined PCA is  $36.1 \pm 21.7 [MPa\sqrt{m}]$ .
5. Nanograined transparent PCA is distinctly rate-sensitive.
6. The fractographic study reveals that for dynamically broken specimens, a unique fracture micromechanism operates that is related to the high dynamic initiation fracture toughness values.
7. Numerical simulations were carried out that show the combined toughening role of the crack-front geometrical perturbation and the kinetic energy imparted to the specimen.
8. Since similar fracture toughness values are measured using two radically different test geometries for the same material, one can tentatively conclude that the dynamic initiation toughness is a material property.

### Acknowledgments

Dr. A. Dorogoy is kindly acknowledged for many stimulating discussions and assistance with the finite element model. Dr. M. Pascucci is acknowledged for kindly providing the PCA specimens.

## TABLES

Table 1: Mechanical properties of transparent nano-grained Alumina, as reported by the manufacturer, (Parish, et al., 2005).

transparent nano-grain Alumina	E [GPa] Young's modulus	$\nu$ Poisson ratio	$\rho$ [ $kg / m^3$ ] density
	387	0.22	3970

Table 2: Single Edge Precracked Beam (SEPB) fracture toughness compared with Indentation Fracture (IF) toughness measurements of similar material.

Material	Test Method	$K_{Ic}^s$ [ $MPa\sqrt{m}$ ]
CeraNova PCA, current study (9 spec)	SEPB	3.12±0.075
CeraNova PCA, (Parish, et al., 2005)	IF	3.30±0.120
Sub- $\mu m$ $Al_2O_3$ , (Krell, et al., 2003b)	IF	~3.50

Table 3: Comparison of dynamic fracture toughness results for various ceramics.

Material	$K_{Ic}^s$ [ $MPa\sqrt{m}$ ]	$K_{Ic}^d$ [ $MPa\sqrt{m}$ ]	$\dot{K}_d$ [ $MPa \cdot \sqrt{m} \cdot s^{-1}$ ]
CeraNova PCA, current study (15 spec)	3.12±0.075	36.1±21.7	$> 10^6$
SiC-N, (Weerasooriya, et al., 2006)	4.75±0.25	7.5±2.0	$10^5$
$Al_2O_3$ , (Suresh, et al., 1990)	2.70	3.5	$10^6$

Table 4: Description of elements types, average size of the elements and type of crack front shapes that were used in FE analyses.

Loading Type	Analyses Type	Crack Front Type	Element Type	Total Number of Elements	$h_{av}^e$ [m]	$h_{av}^e/a$
Static	ABAQUS Standard	Straight	C3D8R <sup>1</sup>	33582	$38.6 \cdot 10^{-6}$	$7.95 \cdot 10^{-3}$
		Triangular	C3D4 <sup>2</sup>	92106	$38.8 \cdot 10^{-6}$	$7.98 \cdot 10^{-3}$
Dynamic	ABAQUS Explicit	Straight	C3D8R <sup>1</sup>	32820	$40.0 \cdot 10^{-6}$	$17.75 \cdot 10^{-3}$
		Triangular	C3D4 <sup>2</sup>	72331	$32.5 \cdot 10^{-6}$	$14.23 \cdot 10^{-3}$

1. C3D8R – is an 8-node linear brick element which uses reduced integration and hourglass control.
2. C3D4 – is 4-node linear tetrahedron element.

$h_{av}^e$  is the average element size near the crack tip and  $a$  is the crack length

Table 5: Numerical simulation results of selected crack advance schemes.  $\Delta A$  is the increment of crack growth and  $t_{fract}$  is the measured fracture time. The values of  $G$  and  $G^*$  are those from the leftmost point in Figure 16 corresponding to the smallest  $\Delta A$ . The contribution of the strain and kinetic energies is evaluated at this point. Note that for the dynamic straight-straight case, the kinetic energy term is dominant while for the perturbed crack-front, its relative contribution is smaller.

Loading regime	Case	$\Delta A$ [m <sup>2</sup> ]	$t_{fract}$ [μs]	$G$ or $G^*$ [N/m]	$\frac{\Delta U}{\Delta A}$ [N/m]	$\frac{\Delta E^k}{\Delta A}$ [N/m]
Static	Straight-straight	$0.6 \times 10^{-7}$	-	23	23	-
Dynamic	Straight-straight	$0.6 \times 10^{-7}$	16.5	2764	155	2609
Dynamic	Fully triangular-straight	$0.3 \times 10^{-7}$	16.5	9776	3710	6066

## FIGURES

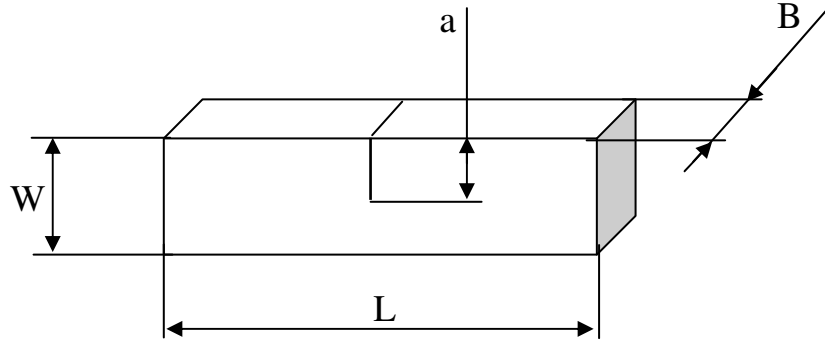
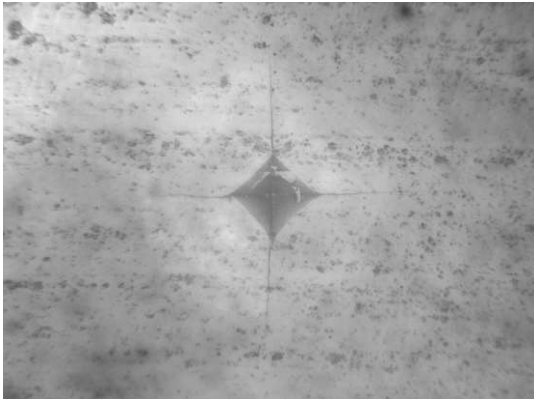
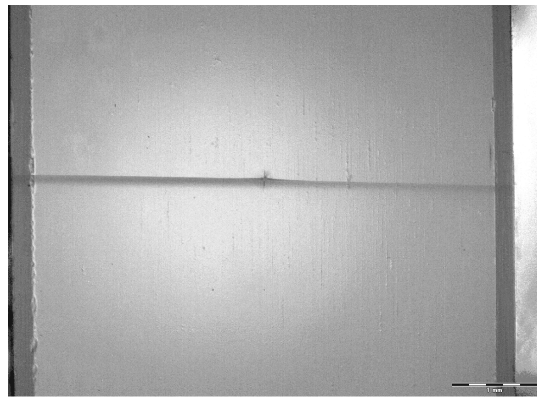


Fig. 1: Specimen dimensions.  $L=45$  [mm] (or 22.5 [mm] for short specimens) is the length,  $W=8$  [mm] is the width and  $B=6$  [mm] is the depth of the PCA specimens. The crack length is denoted by  $a$  and optically measured post-mortem.



**a.**



**b.**

Fig. 2: **a.** Vickers indentation on polished PCA specimen. The cracks emanating from the corners of the indent can be clearly seen. **b.** A typical precrack on PCA specimen. The picture was taken with specimen through-lighting. Note the translucency of the specimen.

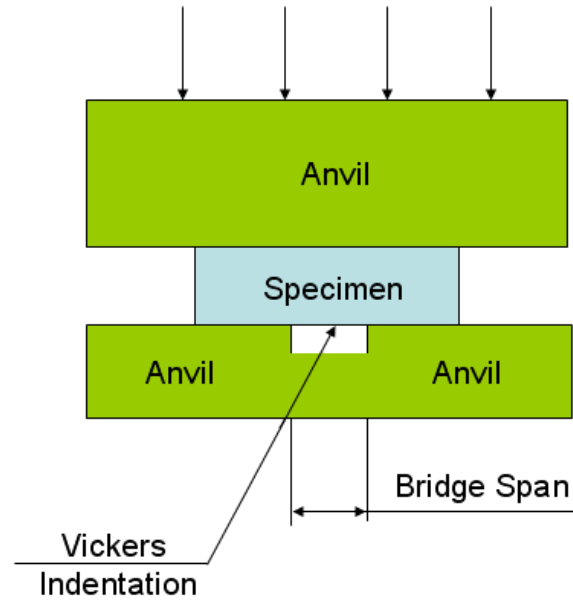


Fig. 3: Double anvil fixture that was used to introduce straight precrack from Vickers indentation into the specimens. By controlling the bridge span and Vickers indentation load one can affect the precrack length.

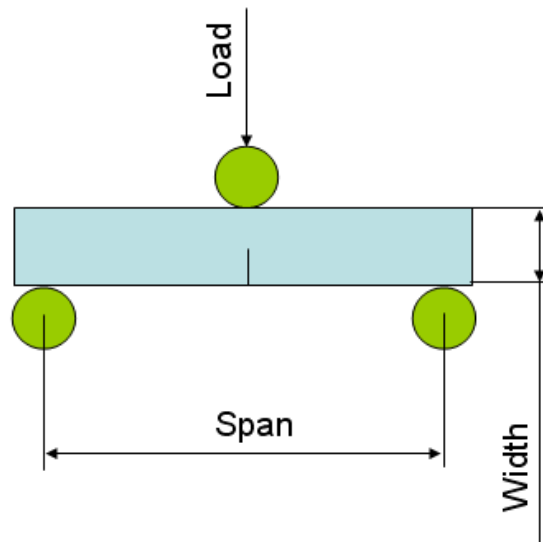


Fig. 4: Schematic drawing of 3-point bending test. Span to width relation should be chosen according to ASTM 1421 (1999) standard, for the results reported in this study span to width ratio was 5.

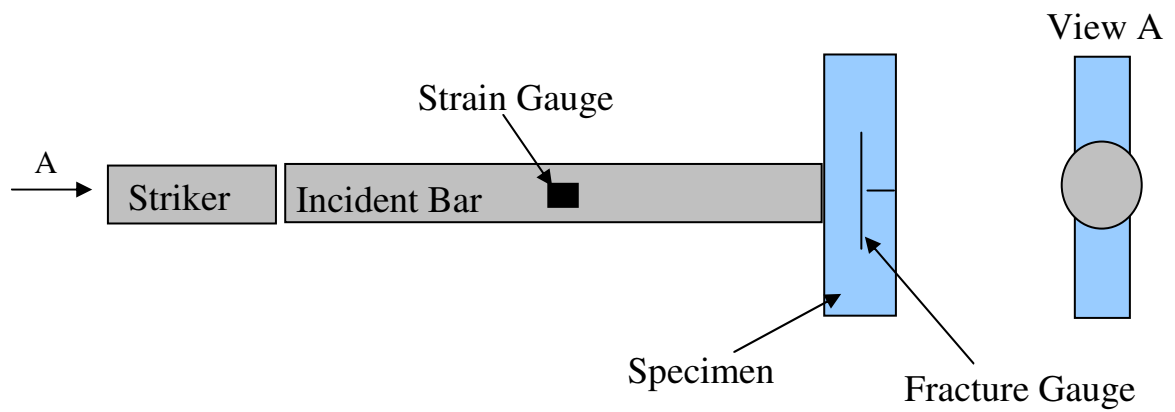


Fig. 5: Schematic drawing of one-point impact experimental setup. The incident bar dimensions were chosen to match the specimen height. The fracture gauges were painted by silver paint on both sides of the specimen in the vicinity of the crack tip.

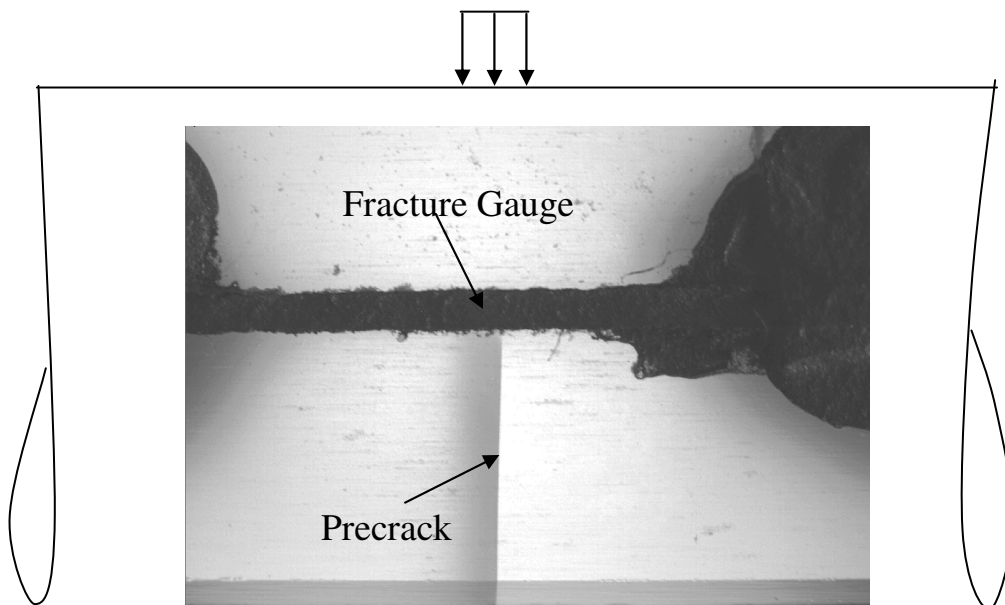


Fig. 6: Precracked specimen with fracture gauge painted near the crack tip. The picture was taken with specimen through-lighting.

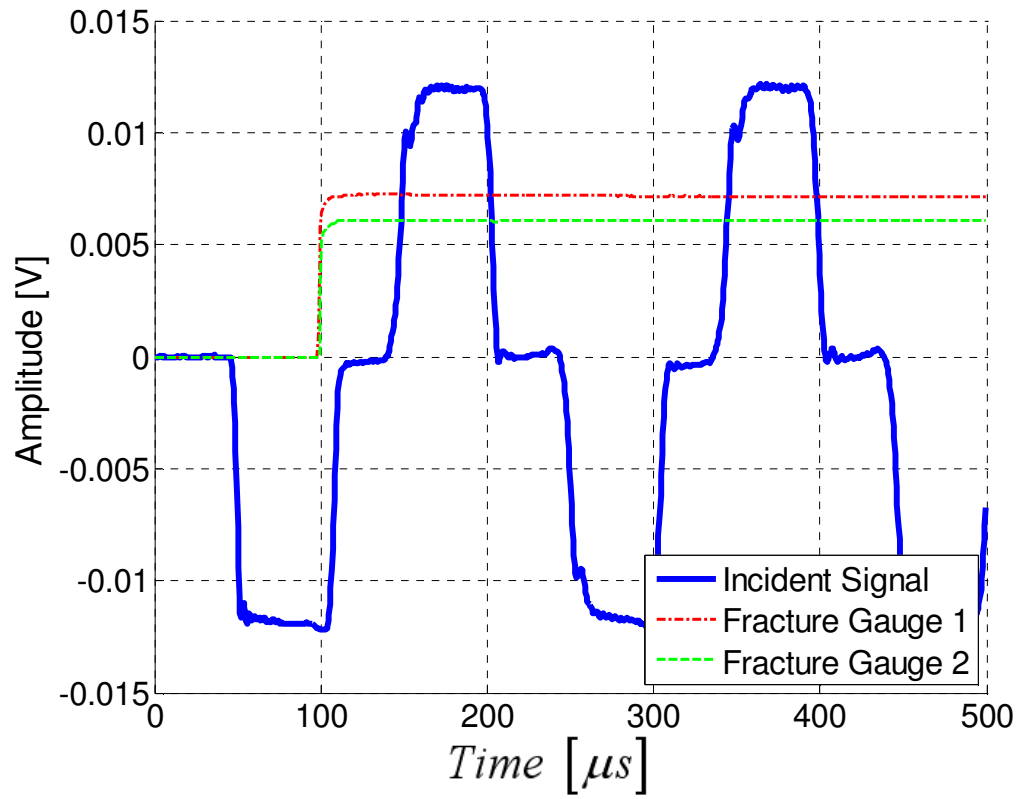


Fig. 7a: Typical incident and reflected pulses, and fracture gauges' readings versus time. Note the excellent agreement between two fracture gauges' readings, (Alumina Sp7-1).



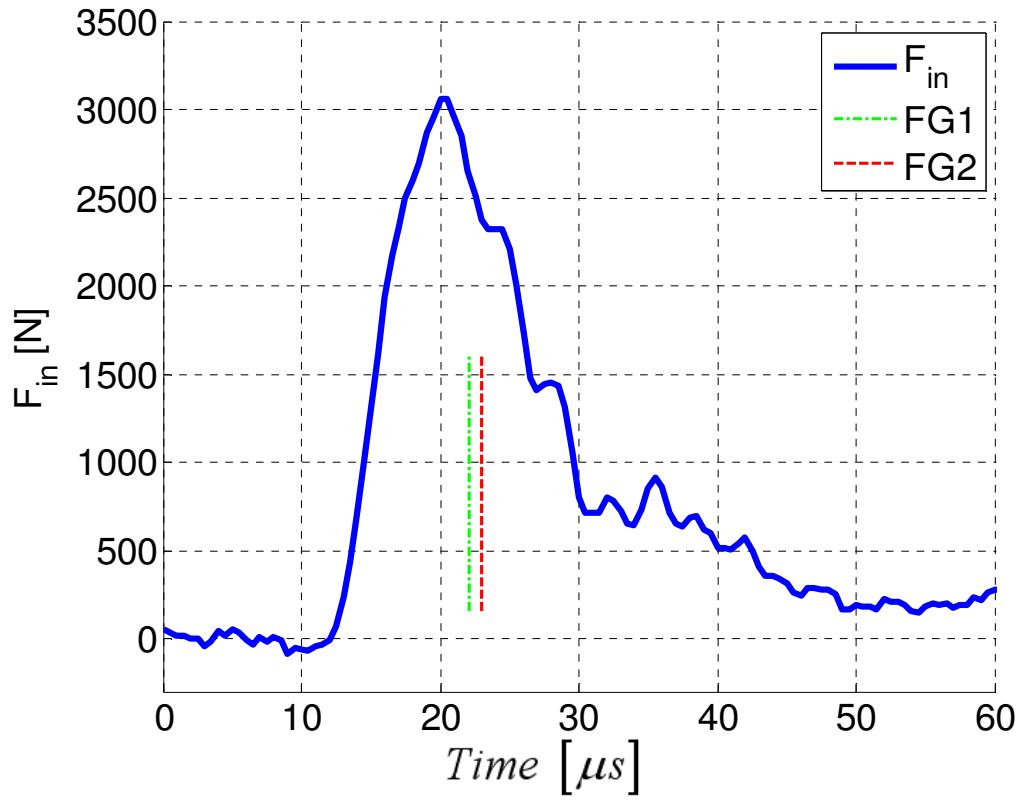


Fig. 7b: The actual force-time relationship for a typical PMMA specimen, (Sp9), after data synchronization and reduction. The two dashed lines show the fracture gauges' readings, showing that the onset of crack propagation actually occurs beyond the peak load.

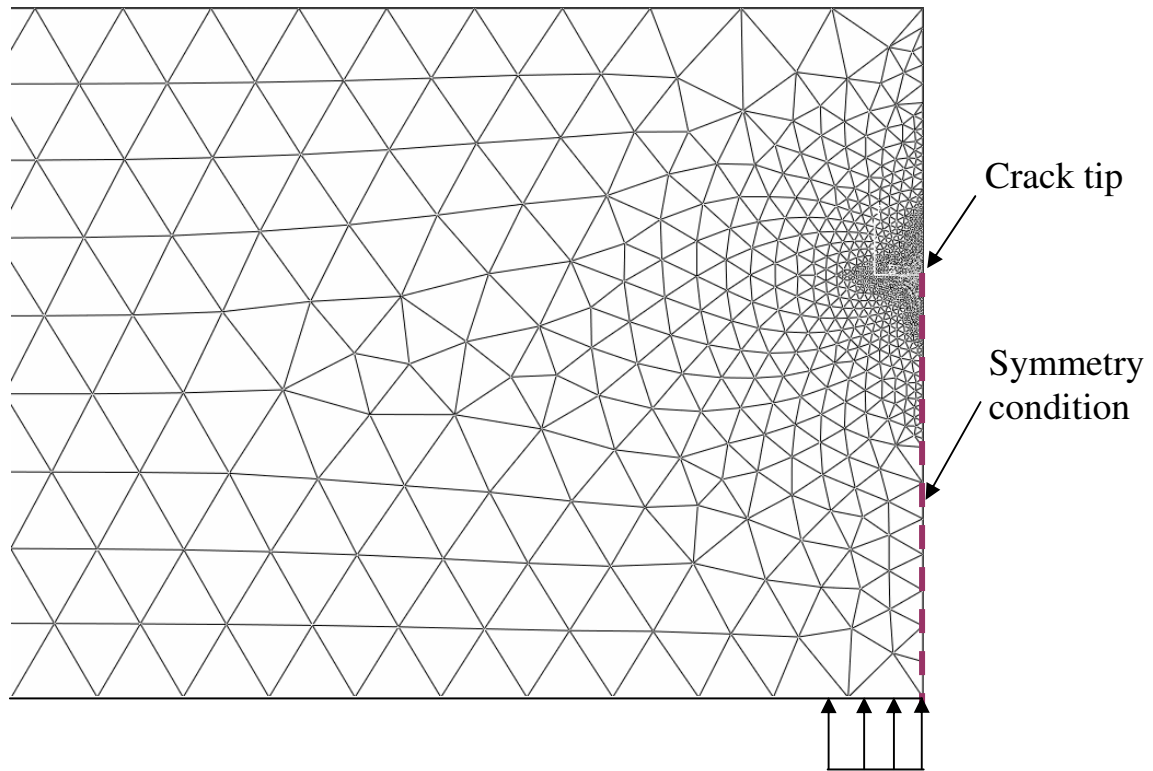


Fig. 8: Close up on meshed 2D plain strain alumina half-specimen along with the boundary condition. The acting force was modeled as pressure acting on the equivalent area.

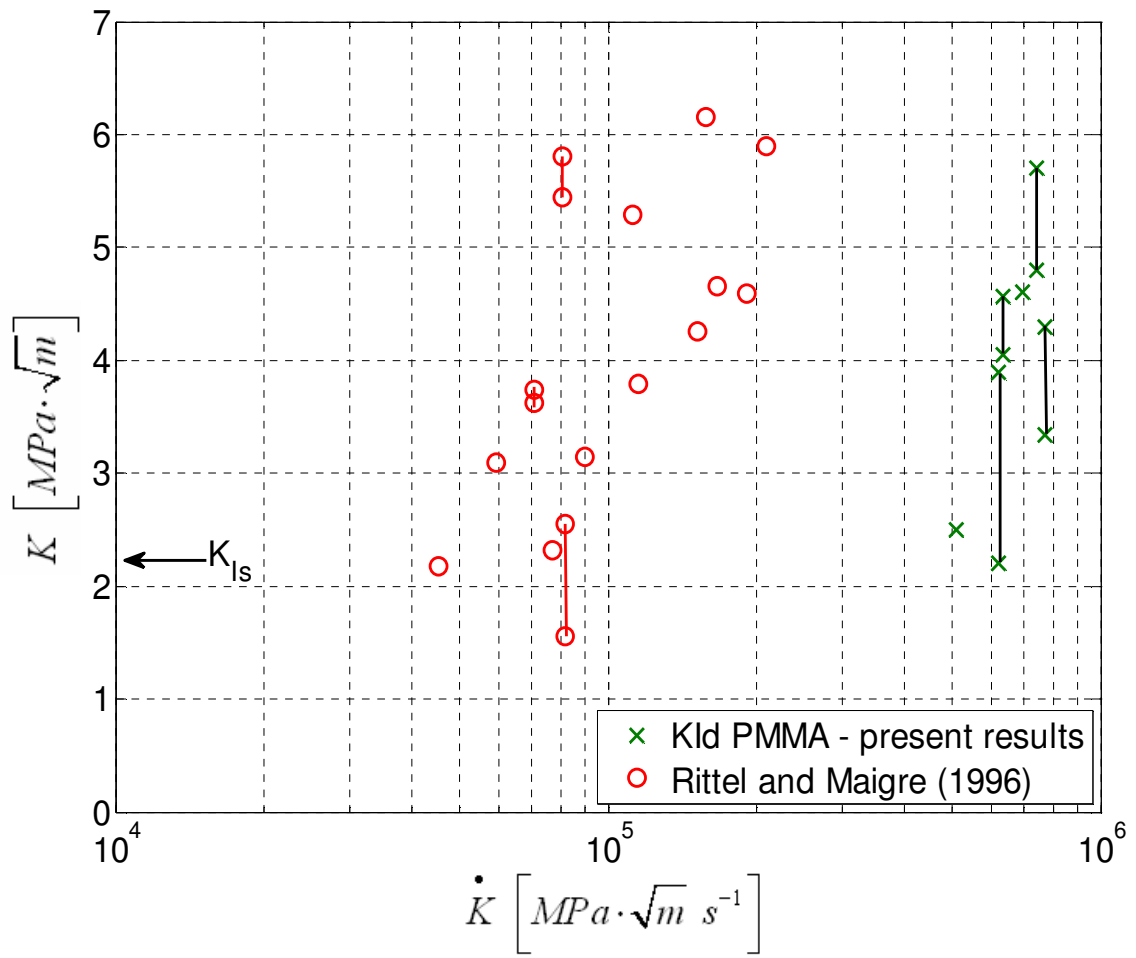


Fig. 9: Comparison of PMMA fracture toughness values from present study to those from Rittel and Maigre (1996) versus stress intensity rate. Note the similar values of  $K$ , irrespective of  $\dot{K}$  for two different specimen geometries.

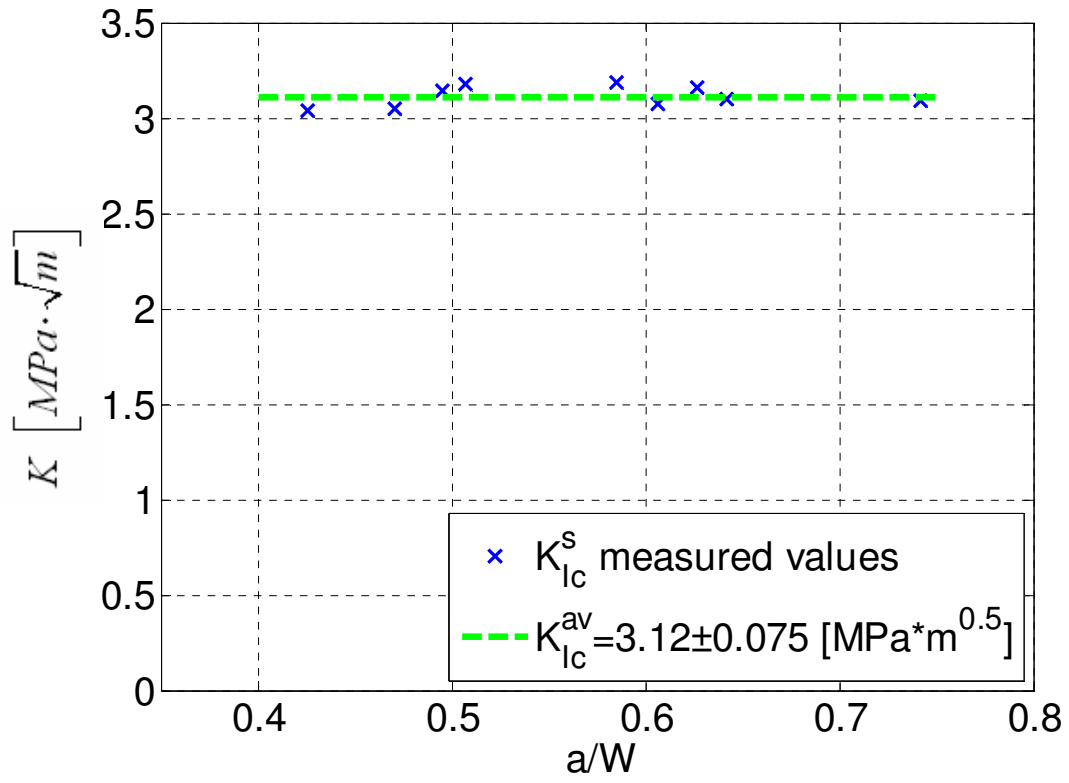


Fig. 10: Measured static fracture toughness values versus non-dimensional crack length. The green broken line shows the average fracture toughness value of 9 measurements. According to the plot there is no evidence for R-curve behavior.

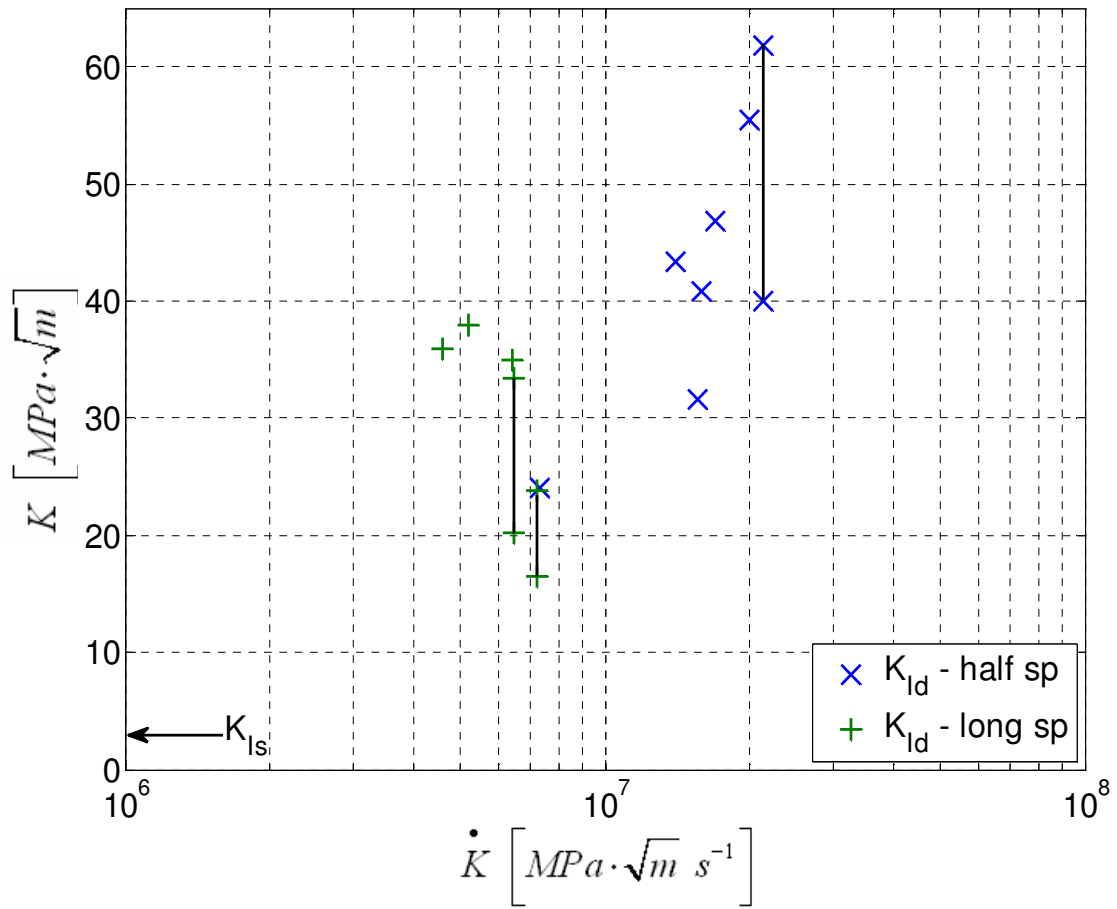


Fig. 11: PCA fracture toughness values versus stress intensity rate. The letter "s" stands for static tests and the letter "d" stands for dynamic tests. Note the similar values of  $K$ , over a range of  $\dot{K}$  for two different specimen geometries (long and half-bars).

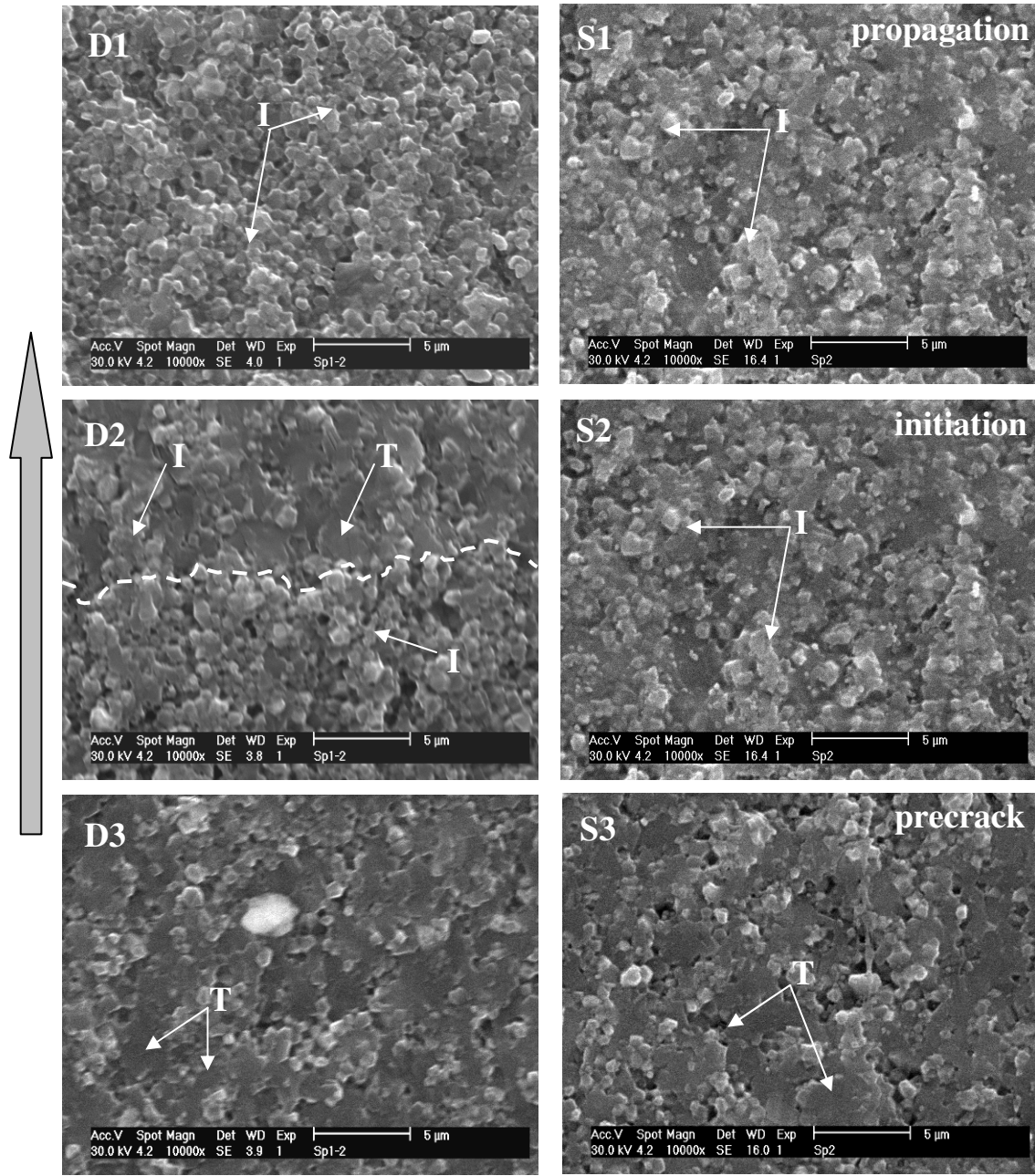


Fig. 12: Comparison of fractographic pictures of selected areas at the dynamically and statically broken specimens, at the same level of magnification. The solid arrow shows the fracture direction. Pictures D1-D3 shows different areas of dynamically broken specimen (Sp1-2). Pictures S1-S3 shows different areas of statically broken specimen (Sp2). D3 and S3: precrack; D2 and S2: fracture initiation, white broken line on picture D2 outlines the precrack front, showing the distinct difference in fracture mechanism between precrack and fracture initiation; D1 and S1: fracture propagation. "T" stands for transgranular fracture, "I" for intergranular fracture.

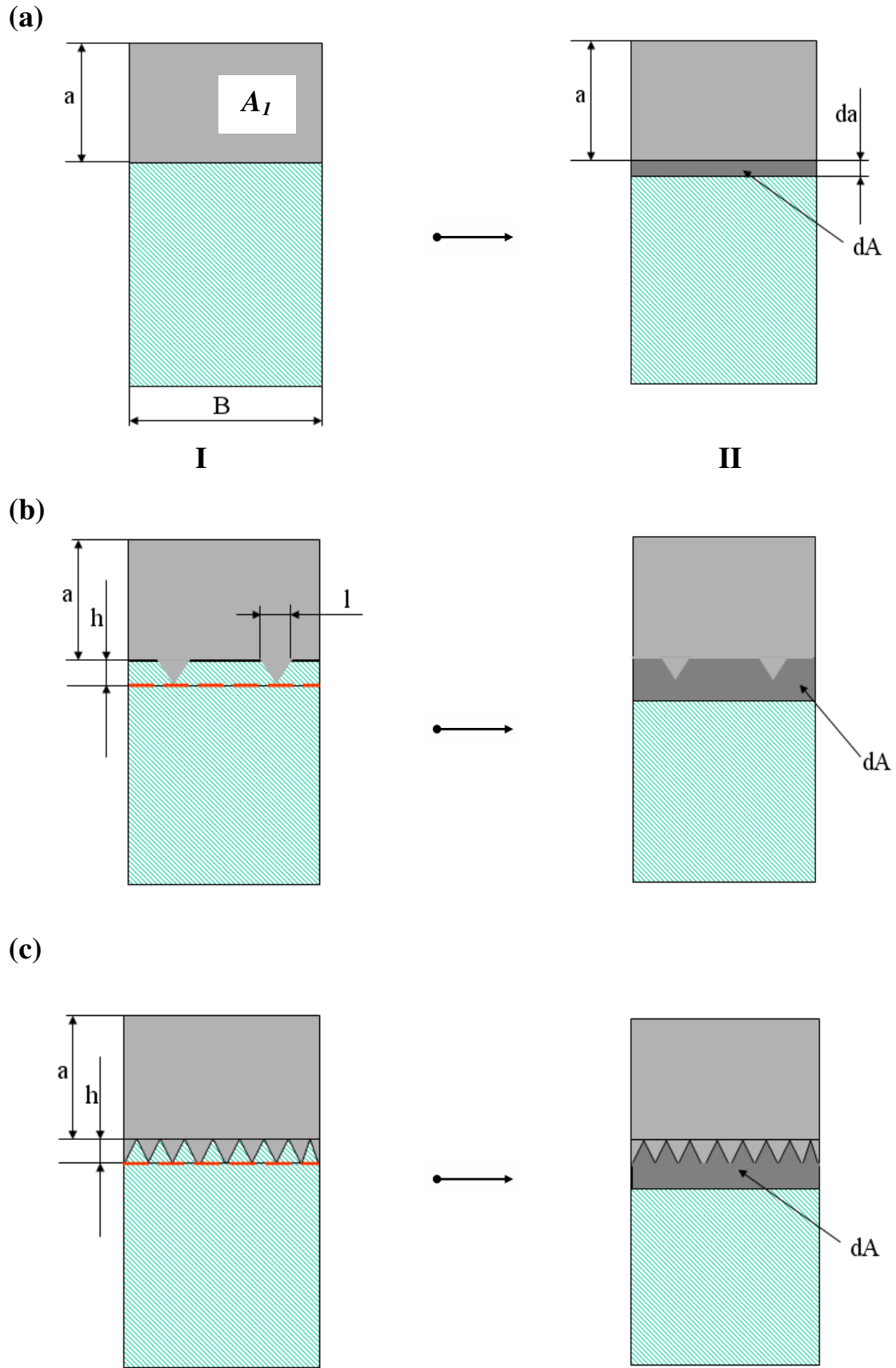


Fig. 13: Schematic representation of the various investigated schemes for crack advance. The crack evolution is from left to right. (a) Case 1.1: straight-straight. (b) Case 3.1: coarse triangular (2) -straight, and (c) Case 2.1: fully triangular-straight.

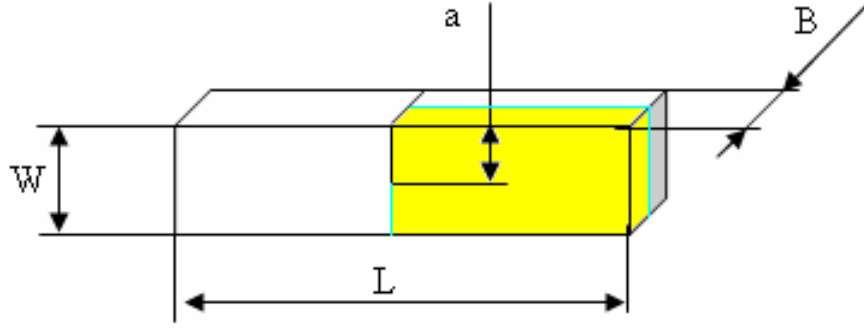


Fig. 14: The quarter-specimen (shadowed), which was simulated numerically by applying two symmetry conditions.

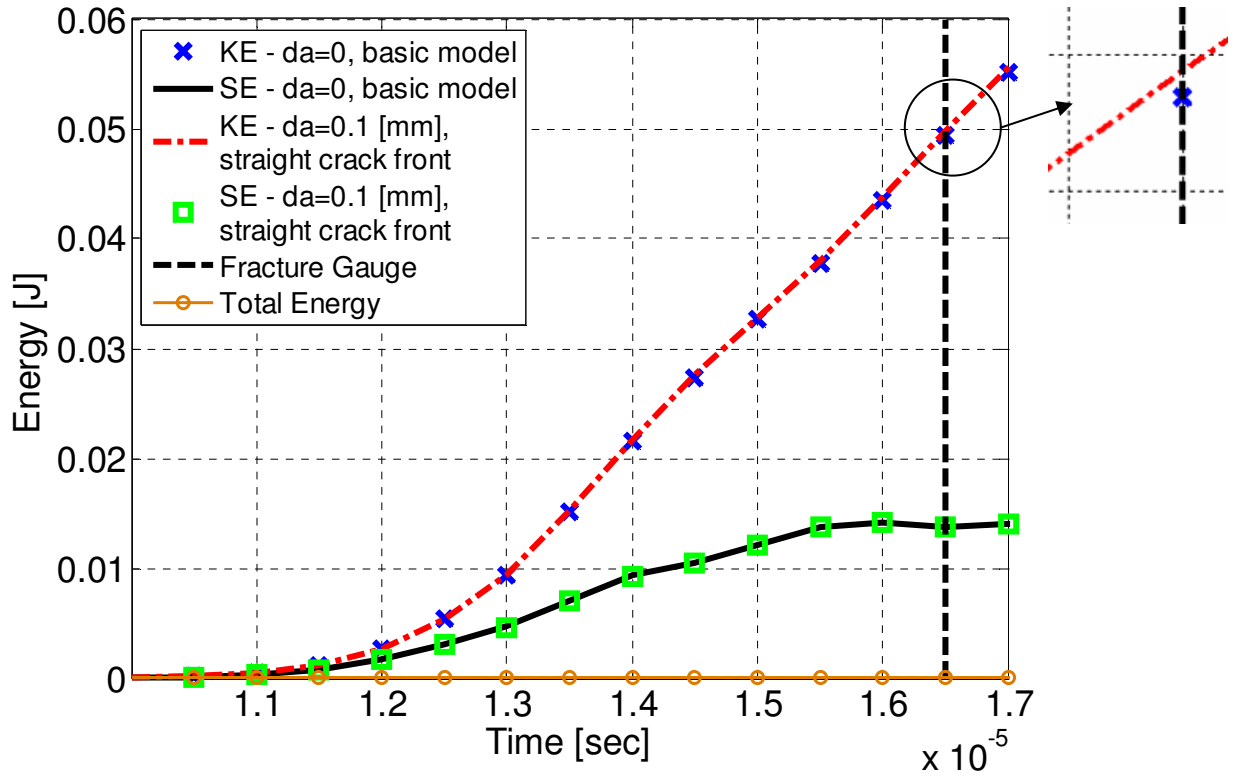


Fig. 15: Comparison of the kinetic and strain energies, KE and SE respectively, during the impact simulation versus time for the basic model (no crack area increment) and for  $da = 0.1 \text{ [mm]}$ , straight crack front advance. The dotted line is the total energy during the impact. Zero total energy validates the energy conservation during the simulation. The magnified selected area shows that the energies are not identical after crack advance, as might appear from the main plot.



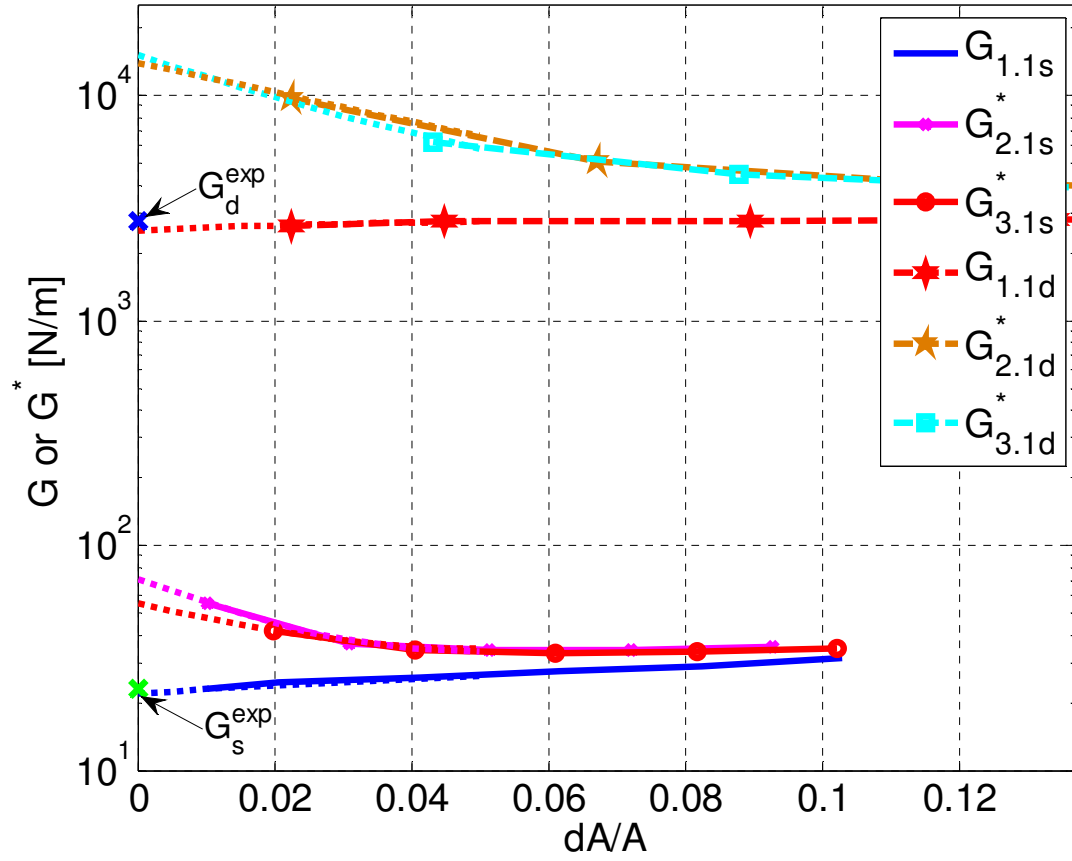


Fig. 16: Comparison of the energy release rate ( $G$ ) and energy criterion ( $G^*$ ) for the static ("s") and dynamic ("d") loadings of cases 1.1 – straight-straight, 2.1 – fully triangular-straight and 3.1 – two triangles-straight, versus normalized crack area increment. Note that the critical value is obtained by extrapolating the curves to  $\Delta A/A \rightarrow 0$ . The measured values are given in Table 5.

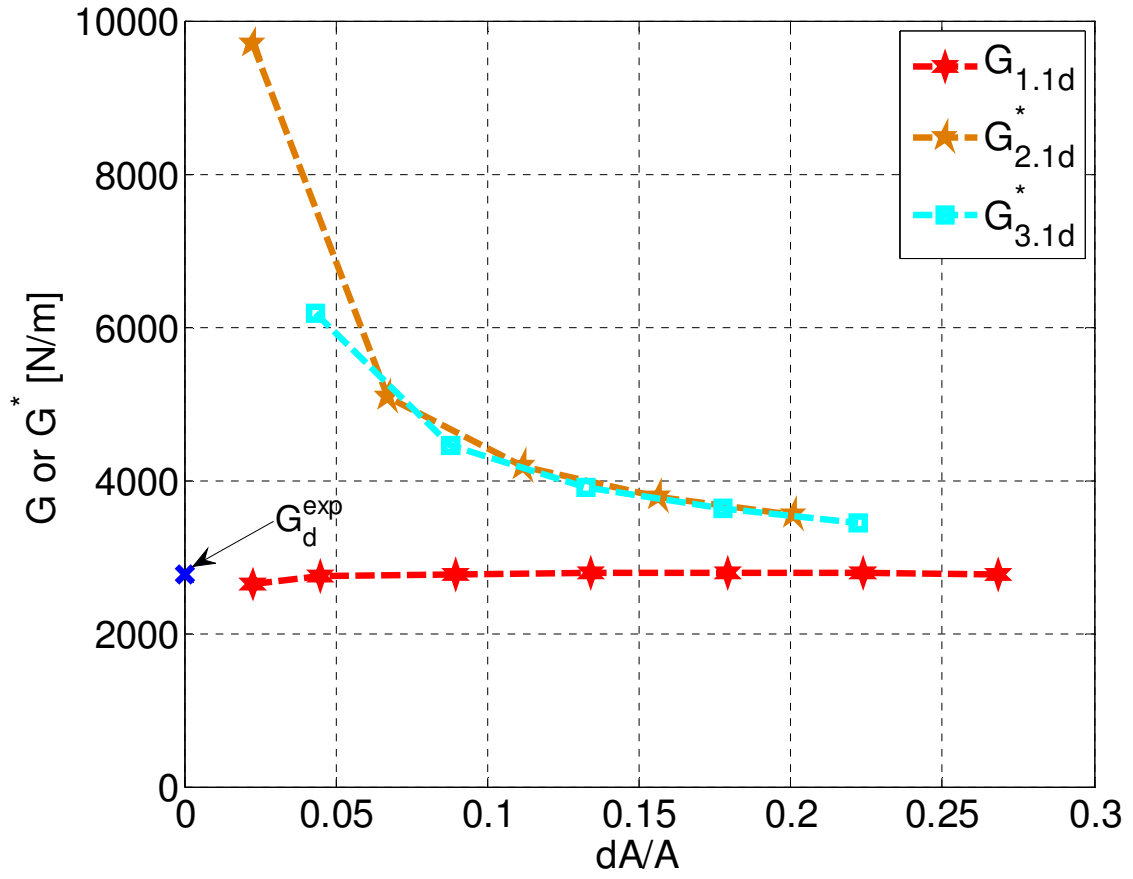


Fig. 17: Comparison of the energy release rate ( $G$ ) and energy criterion ( $G^*$ ) for the dynamic loading of cases 1.1 – straight-straight, 2.1 – two triangles-straight and 3.1 – fully triangular-straight, versus normalized crack area increment. The measured value is given in Table 5.

## REFERNCES

- ABAQUS, 2008. p. Dassault Systems.
- Anderson, T.L., 1995. Fracture Mechanics: Fundamentals and Applications. CRC Press.
- Aoki, S., Kimura, T., 1993. Finite element study of the optical method of caustic for measuring impact fracture toughness. J. Mech. Phys .Solids 41 (3), 413-425.
- ASTM-C1327, 1999. Standard Tests Method for Vickers Indentation Hardness of Advanced Ceramics.
- ASTM-C1421, 1999. "Standard Test Methods for Determination of Fracture Toughness of Advanced Ceramics at Ambient Temperature."
- ASTM-E3 .1990 ,99Standard Test Method for Plane-Strain Fracture Toughness of Metallic Materials.
- Baron, I., Beals, J., Leatherman, G.L., Murray, C.M., 1990. Fracture-Toughness of Ceramic Precracked Bend Bars. Journal of the American Ceramic Society 73 (8), 2519-2522
- Broberg, K.B., 2002. Constant velocity crack propagation - dependence on remote load. Int. J. Solids & Structures 39, 6403-6410.
- Chandra, D., Krauthammer, T., 1995. Dynamic Effects on Fracture-Mechanics of Cracked Solids. Engineering Fracture Mechanics 51 (5), 809-822.
- Gao, H., Rice, J.R., 1989. First-order perturbation analysis of crack trapping by arrays of obstacles J. Appl. Mech. 56, 828-836.
- Gdoutos, E., 2005. Fracture Mechanics: An Introduction. Springer.
- Giovanola, J.H., 1986. Investigation and Application of the One-Point-Bend Impact Test. ASTM, Philadelphia, PA, USA, pp. 307-328.
- Gogotsi, G.A., 2003. Fracture toughness of ceramics and ceramic composites. Ceramics International 29 (7), 777-784.
- Grendahl, S., Bert, R., Cho, K., Bar-On, I., 2000. Effects of residual stress and loading geometry on single-edge precracked-beam (SEPB) fracture-toughness test results. Journal of the American Ceramic Society 83 (10), 2625-2627.
- Jiang, F.C., Vecchio, K.S., 2009. Hopkinson Bar Loaded Fracture Experimental Technique: A Critical Review of Dynamic Fracture Toughness Tests. Applied Mechanics Reviews 62 (6), 39.
- Kalthoff, J.F., 1986. Fracture-Behavior under High-Rates of Loading. Engineering Fracture Mechanics 23 (1), 289-298.
- Kaplan, W.D., Rittel, D., Lieberthal, M., Frage, N., Dariel, M.P., 2004. Static and dynamic mechanical damage mechanisms in TiC-1080 steel cermets. Scripta Materialia 51 (1), 37-41.

Kolsky, H., 1949. An investigation of the mechanical properties of materials at very high rates of loading. *Proceedings of the Physical Society. Section B* 62 (11), 676-700.

Krell, A., Blank, P., Ma, H.W., Hutzler, T., Nebelung, M., 2003a. Processing of high-density submicrometer Al<sub>2</sub>O<sub>3</sub> for new applications. *Journal of the American Ceramic Society* 86 (4), 546-553.

Krell, A., Pippel, E., Woltersdorf, J., Burger, W., 2003b. Subcritical crack growth in Al<sub>2</sub>O<sub>3</sub> with submicron grain size. *Journal of the European Ceramic Society* 23 (1), PII S0955-2219(0902)00072-00079.

Liu, C., Knauss, W.G., Rosakis, A.J., 1998. Loading rates and the dynamic initiation toughness in brittle solids. *Int. J. Fracture* 90, 103-118.

Nose, T., Fujii, T., 1988. Evaluation of Fracture-Toughness for Ceramic Materials by a Single-Edge-Pre-cracked-Beam Method. *Journal of the American Ceramic Society* 71 (5), 328-333.

Parish, M.V., Pascucci, M.R., Rhodes, W.H., 2005. Aerodynamic IR domes of polycrystalline alumina. *Window and Dome Technologies and Materials IX* 5786, 195-205.

Ponson, L., 2009. Depinning transition in failure of inhomogeneous brittle materials. *Physical Review Letters* 103 (5), 055501.

Quinn, G.D., Bradt, R.C., 2007. On the Vickers indentation fracture toughness test. *Journal of the American Ceramic Society* 90 (3), 673-680.

Ritchie, R.O., Knott, J.F., Rice, J.R., 1973. On the relationship between critical tensile stress and fracture toughness in mild steel. *J. Mech. Phys. Solids* 21, 395-410.

Rittel, D., 2006. Dynamic Crack Initiation Toughness. In: Shukla, A. (Ed.), *Dynamic fracture mechanics*. World Scientific, New Jersey, p. 66.

Rittel, D., Frage, N., Dariel, M.P., 2005. Dynamic mechanical and fracture properties of an infiltrated TiC-1080 steel cermet. *International Journal of Solids and Structures* 42 (2), 697-715.

Rittel, D., Maigre, H., 1996. An investigation of dynamic crack initiation in PMMA. *Mechanics of Materials* 23 (3), 229-239.

Rittel, D., Pineau, A., Clisson, J., Rota, L., 2002a. On testing of Charpy specimens using the one-point bend impact technique. *Experimental Mechanics* 42 (3), 247-252.

Rittel, D., Rosakis, A.J., 2005. Dynamic fracture of beryllium-bearing bulk metallic glass systems: A cross-technique comparison. *Engineering Fracture Mechanics* 72 (12), 1905-1919.

Rittel, D., Tanguy, B., Pineau, A., Thomas, T., 2002b. Impact fracture of a ferritic steel in the lower shelf regime. *International Journal of Fracture* 117 (2), 101-112.

Rittel, D., Weisbrod, G., 2001. Dynamic fracture of tungsten base heavy alloys. *International Journal of Fracture* 112 (1), 87-98.

- Shukla, A., 2006. Dynamic Fracture Mechanics. World Scientific Publishing Company.
- Suresh, S., Nakamura, T., Yeshurun, Y., Yang, K.H., Duffy, J., 1990. Tensile Fracture-Toughness of Ceramic Materials - Effects of Dynamic Loading and Elevated-Temperatures. *Journal of the American Ceramic Society* 73 (8), 2457-2466.
- Weerasooriya, T., Moy, P., Casem, D., Cheng, M., Chen, W., 2006. A four-point bend technique to determine dynamic fracture toughness of ceramics. *Journal of the American Ceramic Society* 89 (3), 990-995.
- Weisbrod, G., Rittel, D., 2000. A method for dynamic fracture toughness determination using short beams. *International Journal of Fracture* 104 (1), 89-103.
- Yokoyama, T., 1993. Determination of Dynamic Fracture-Initiation Toughness Using a Novel Impact Bend Test Procedure. *Journal of Pressure Vessel Technology-Transactions of the Asme* 115 (4), 389-397.
- Zhang, C.H., Gross, D., 1992. Pulse shape effects on the dynamic stress intensity factor. *Int. J. Fracture* 58 (1), 55-75.